sPHENIX | Report

tag: sPH-CONF-JET-2025-01
version: 1.0
DOI: unspecified
date: April 6, 2025

sPHENIX Conference Note

...

Measurement of dijet imbalance (x_J) and acoplanarity ($\Delta\phi$) in $p + p$ collisions at $\sqrt{s} = 200$ GeV with the sPHENIX detector

sPHENIX Collaboration

Abstract

This sPHENIX Conference Note details the measurement of dijet imbalance (x_J) and acoplanarity ($\Delta\phi$) in $p + p$ collision data at $\sqrt{s} = 200$ GeV taken with the sPHENIX detector in 2024 at the Relativistic Heavy Ion Collider (RHIC). Jets are reconstructed using the anti-k_t algorithm with $R = 0.4$ from electromagnetic and hadronic calorimeter energy information. Selections are made on leading jets in exclusive regions of $20.9 \leq p_{T,1} < 31.2$ GeV, $31.2 \leq p_{T,1} < 40.7$ GeV, and $40.7 \leq p_{T,1} < 60.2$ GeV and subleading jets with $p_{T,2} > 9.4$ GeV opposite the leading jet ($\Delta\phi > 3\pi/4$). The distribution of $x_J = p_{T,2}/p_{T,1}$ is calculated and unfolded for detector effects back to the truth-particle-level distribution. The $\Delta\phi$ distribution is calculated and corrected for bin migration and detector resolution effects. The x_J and $\Delta\phi$ distributions are normalized per jet pair satisfying the kinematic selections and correspond to minimum bias $p + p$ events satisfying the sPHENIX Minimum Bias Detector trigger requirements. The unfolded x_J and corrected $\Delta\phi$ results are then compared with Monte Carlo PYTHIA-8 and HERWIG-7.3 generator calculations.

1 Introduction

Measurements of dijet production have a long history in heavy-ion physics – for a review see Ref. [1]. One of the first measurements confirming the creation of the Quark-Gluon Plasma (QGP) in nucleus-nucleus collisions at the Large Hadron Collider (LHC) was of an increased dijet asymmetry, defined as $A_J = (p_{\mathrm{T},1} - p_{\mathrm{T},2})/(p_{\mathrm{T},1} + p_{\mathrm{T},2})$, in central Pb+Pb events compared with the expectation from $p + p$ collisions by ATLAS [2]. One proposed explanation is that the asymmetry is caused by the differential energy loss of the two jets [3]. Depending on the production point of the dijet in the plasma, the path lengths traversed by each should be generally anti-correlated. Thus, the different amounts of energy loss should result in a larger proportion of highly asymmetric emerging jet pairs, and lead to a broadening of the A_J distribution. However, others have argued that the modification of the A_J distribution is additionally sensitive to the large fluctuations in jet-by-jet energy loss [4]. Many follow-up measurements were made, including a confirmation and additional studies by CMS [5, 6]. In Ref. [7], ATLAS first used a 2-D unfolding procedure to correct for detector effects, and future ATLAS papers instead reported $x_J = p_{\mathrm{T},2}/p_{\mathrm{T},1}$. Follow-up measurements in LHC Run-2 data explored the x_{J} distribution at a higher Pb+Pb collision energy [8] and for different cone sizes [9] to test the interplay with recovery of radiated energy. Distributions of the dijet azimuthal difference, $\Delta\phi = \phi_1 - \phi_2$, are potentially sensitive to several physics effects, including initial- and final-state k_T scattering, next-to-leading-order (NLO) radiation, and the possible large-angle scattering of jet partons off of QGP particles or structures [10].

Dijet correlation measurements are expected to be valuable probes of the QGP produced at the Relativistic Heavy Ion Collider (RHIC) at Brookhaven National Laboratory (BNL), and were one of several original motivations for the sPHENIX experiment [11, 12]. Due to the smaller relative contribution from higher-order processes, dijet p_{T} and $\Delta\phi$ distributions have a tighter initial correlation in $p + p$ collisions at RHIC energies than at the LHC, thus increasing the sensitivity of these observables to modification by medium effects in central Au+Au collisions. The large sPHENIX acceptance, hadronic calorimeter, and high-statistics dataset make sPHENIX well-equipped to perform these measurements. A previous measurement by STAR [13] used jets reconstructed with charged tracks and electromagnetic calorimeter towers with "hard-core" selections to investigate the p_{T} balance of jets in Au+Au collisions. However, those results were not unfolded for detector effects. Thus, the present measurement in sPHENIX serves as the first at RHIC with full-calorimeter jets over a broad kinematic range and unfolded to the truth-particle level. This measurement establishes the $p + p$ data baseline for upcoming measurements in Au+Au and evaluates the modeling of these distributions in Monte Carlo (MC) generators for theoretical comparisons.

This sPHENIX conference note presents the dijet imbalance x_J distributions with selections on the leading jet in exclusive regions of $20.9 \leq p_{T,1} < 31.2$ GeV, $31.2 \leq p_{T,1} < 40.7$ GeV, and $40.7 \leq p_{T,1} < 60.2$ GeV and on the subleading jet $p_{T,2} > 9.4$ GeV that is opposite the leading jet ($\Delta\phi > 3\pi/4$). The dijet acoplanarity, $\Delta\phi$, is presented with the same leading jet selections in addition to subleading jet selections of $9.4 \leq p_{T,2} < 16.8$ GeV, $16.8 \leq p_{T,2} < 20.9$ GeV, $20.9 \leq p_{T,2} < 31.2$ GeV with the same leading $p_{T,1}$ bin $31.2 \leq p_{T,1} < 40.7$ GeV.

2 sPHENIX detector

sPHENIX [11, 12] is a new detector at RHIC designed to measure jet and heavy-flavor probes of the quark-gluon plasma (QGP) created in Au+Au collisions at the Relativistic Heavy-Ion Collider (RHIC) [14]. A precision tracking system enables measurements of heavy-flavor and jet-substructure observables while the electromagnetic and hadronic calorimeter system is crucial for measuring the energy of jets and identifying direct photons and electrons.

Going outwards starting from the beam line, sPHENIX comprises the following subsystems [15]: the MAPS-based Vertex Detector (MVTX); the INTermediate Tracker (INTT); the Time Projection Chamber (TPC) [16]; the Time Projection Chamber Outer Tracker (TPOT) [17]; the Electromagnetic Calorimeter (EMCAL) [18, 19]; the Inner Hadronic Calorimeter (IHCAL) [19]; the 1.4 T superconducting solenoid magnet [20] and the Outer Hadronic Calorimeter (OHCAL) [19]. Except for TPOT, all detectors have full azimuthal coverage and span $|\eta| < 1.1$ in pseudorapidity. sPHENIX also includes a number of forward detectors, namely the Minimum Bias Detectors (MBD), the sPHENIX Event Plane Detectors (sEPD), and the Zero Degree Calorimeters (ZDC), that includes the Shower Maximum Detector (SMD).

sPHENIX began its commissioning process in RHIC Run-2023 with Au+Au collisions at $\sqrt{s_{\mathrm{NN}}} = 200$ GeV. During RHIC Run-2024, sPHENIX collected a large sample of transversely polarized $p + p$ physics data at $\sqrt{s} = 200$ GeV alongside a smaller sample of Au+Au data to complete its commissioning phase in that collision system.

3 Analysis Procedure

3.1 Event Selection

The data used for this dijet analysis are from Run 2024 $p + p$ $\sqrt{s} = 200$ GeV running and utilize both jet and minimum bias (MB) triggers. The jet trigger requires a combined EMCAL and HCal energy threshold of 10 GeV in a region of $\Delta\eta \times \Delta\phi = 0.8 \times 0.8$, along with a coincidence of at least one minimum ionizing charge particle in the MBD on both sides, which is the sPHENIX MBD Trigger. The MBD trigger sees $26.0^{+4.5}_{-1.1}$ mb of the total inelastic $p + p$ cross-section of 42 mb. The dijets used in these analysis are a part of the cross-section seen by the minimum bias trigger. Events are required to have a reconstructed vertex within the z-vertex range of $|z_{\mathrm{vertex}}| < 60$ cm. Only events selected using the Jet 10 trigger are used in this analysis. Events are included if the leading jet $p_{T1} \geq 18.3$ GeV, which is above the 95% efficiency mark of the Jet 10 trigger. The analysis uses data from $p + p$ collisions in two separate beam conditions that have different z_{vtx} distributions, whose differences in jet kinematics are negligible. The integrated luminosity corresponds to approximately 25 pb^{-1}, and is only a subset of the total integrated luminosity sampled in Run 2024.

3.2 Monte Carlo Simulations

The MC PYTHIA-8 [21] event generator is used to populate the response matrix for the unfolding procedure, hence correcting for detector acceptance and inefficiencies. The Detroit PYTHIA-8 tune from Ref. [22] is used, that is matched to RHIC-energy observables. Three PYTHIA-8 samples were generated with different $\hat{p}_{\mathrm{T}}^{\mathrm{min}}$ to enhance the statistics for high p_T dijets. These datasets are generated with the options **HardQCD:all = on** and **PromptPhoton:all = on**. The simulations are generated with a z-vertex distribution representing the 0 mrad crossing angle running. The generated PYTHIA-8 events are then propagated through the full sPHENIX detector using the GEANT-4 simulation package [23] and reconstructed like the data.

The MC HERWIG-7.3 [24] event generator is used in this analysis only for truth-level comparisons with final data results. The Nashville HERWIG-7.3 tune from Ref. [25] is used, that is matched to RHIC-energy underlying event observables. These datasets are generated with the options **JetKtCut:MinKT** set to appropriate values to enhance high p_T jet statistics.

3.3 Jet Object Selection

Jets in this analysis are reconstructed using calorimeter towers in the EMCal and HCal. The inputs to the jet finder are the energies of the individual $\Delta\eta \times \Delta\phi = 0.1 \times 0.1$ inner and outer HCal towers and pseudo-towers for the EMCal – where the pseudo-towers are constructed by summing the energy in the EMCal towers into regions corresponding to the HCal geometry. The towers are assumed to be massless, and the four momentum for each tower is used to reconstruct a pseudojet. These serve as the inputs to reconstruct jets using the anti-k_t algorithm with a jet resolution parameter of R = 0.4, using the FASTJET package [26]. All jets are required to have a jet axis $|\eta_{\mathrm{jet}}| < 0.7$ to ensure full jet containment within the calorimeter system.

3.4 x_J Observable

The x_J distribution is obtained via a projection of the $(p_{T,1}, p_{T,2})$ distribution, following the ATLAS dijet procedure as detailed in Ref. [8]. In this process, if a dijet meets the $p_{T,1}$, $p_{T,2}$ and $\Delta\phi$ kinematic requirements, it is then inserted into the $(p_{T,1}, p_{T,2})$ distribution. The distribution is symmetrized along the $p_{T,1} = p_{T,2}$ line in order to be unfolded, with the contents scaled by a factor of two to conserve the number of dijets. Then, the unfolded $(p_{T,1}, p_{T,2})$ distribution is brought back to its asymmetric form such that $p_{T,1} > p_{T,2}$. The bins of this distribution are logarithmically spaced such that each of the bin contents in $p_{T,1}$ and $p_{T,2}$ can be split into exactly two adjacent x_J bins. If the entry belongs on the diagonal of the distribution, all of the contents are put in the most symmetric x_J bin.

3.5 Unfolding

An unfolding procedure utilizing the iterative Bayesian algorithm [27] in the ROOUNFOLD package [28] is performed to correct for detector efficiency and bin migration in the final x_J results. The response matrix is filled using the PYTHIA-8 simulation described in Section 3.2. A study of the jet energy resolution in data and simulation (described in detail in Appendix A) found that the resolution in data is approximately 10% higher than that in simulation. Therefore, the reconstructed simulation is smeared by an additional 10% in the response matrix. A two-dimensional unfolding of the leading jet $p_{T,1}$ and subleading jet $p_{T,2}$ in logarithmic bins is used, so that a projection of the distribution can produce an unfolded x_J result. All truth level dijet events from primary particles produced during the PYTHIA-8 event generation that meet our dijet requirements are accounted for in the unfolding. The leading truth jet is required to satisfy $p_{T,1} \geq 14$ GeV and the subleading jet to satisfy $p_{T,2} \geq 5$ GeV, with the additional criteria that the azimuthal separation between leading and subleading jet satisfies $\Delta\phi \geq \frac{3\pi}{4}$.

Truth jets are matched to reconstructed jets (meaning jets from the full GEANT-4 [23] simulation and detector response) if their jet axes match within $\Delta R \leq 0.3$. If more than one jet matches, the reconstructed jet of the higher energy is selected. Only the leading and subleading reconstructed jets are considered for truth matching because only these two are considered in the dijet analysis in data. An example response matrix used in the two-dimensional unfolding procedure is shown in Figure 1.

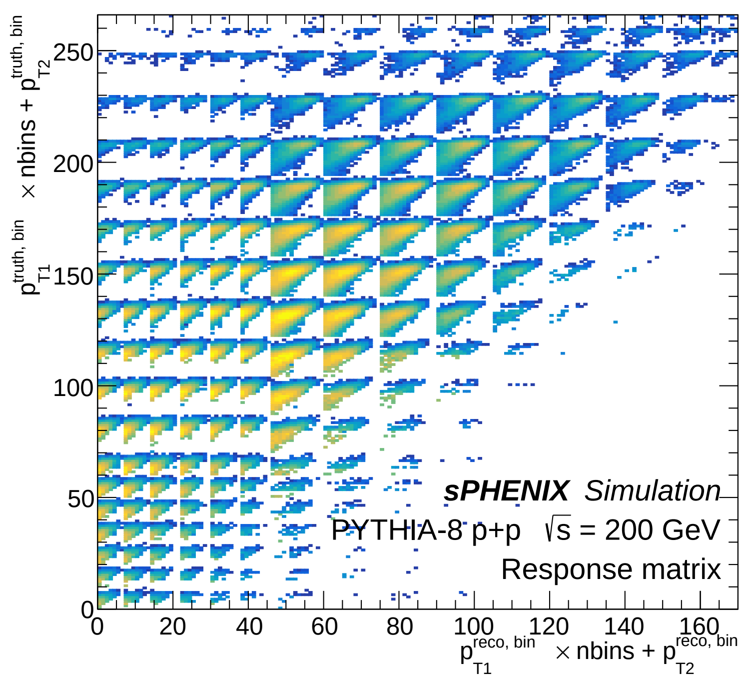

Figure 1: Response matrix trained with PYTHIA-8 and the sPHENIX reconstruction chain.

3.6 $\Delta\phi$ Observable

The $\Delta\phi$ analysis uses corrections that are derived from the $\Delta\phi$ of reconstruction-level and truth-level PYTHIA-8 dijets within each of the three p_{T1} and p_{T2} selections after the jet energy scale calibration. This is to account for bin-migration, ϕ-resolution, and detector efficiency. Figure 2 shows the comparison between the truth level and reconstructed level $\Delta\phi$. The reconstruction-truth correction is the ratio of the two distributions, which is then applied as a bin-by-bin multiplicative factor to the $\Delta\phi$ distributions in data.

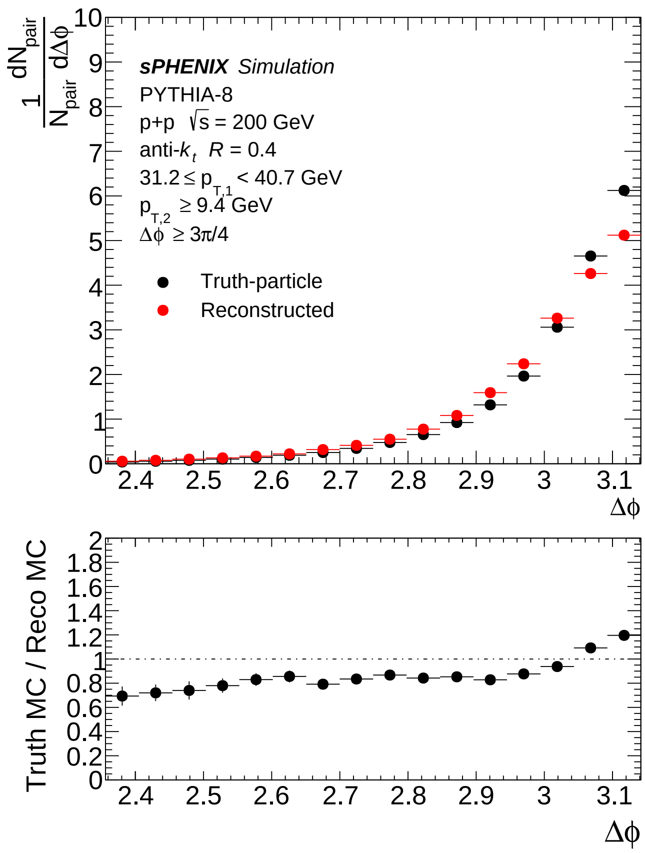

Figure 2: (Top) $\Delta\phi$ of reconstruction-level and truth-level PYTHIA-8 dijets in the leading p_{T1} bin $31.2 \le p_{T1} < 40.7$ GeV selection. (Bottom) Correction factor applied to $\Delta\phi$ distribution in data.

4 Systematic Uncertainties

The systematic uncertainties included in the x_J analysis are from uncertainties in (i) the jet energy scale (JES), (ii) the jet energy resolution (JER), (iii) matching MC to real data jet event multiplicity, and (iv) sensitivity to the prior for the unfolding. The dominant uncertainty is from the JER uncertainty, whose determination is detailed in Appendix A, while the JES uncertainty largely cancels in the ratio x_J. The breakdown of these uncertainties is shown in Figure 3.

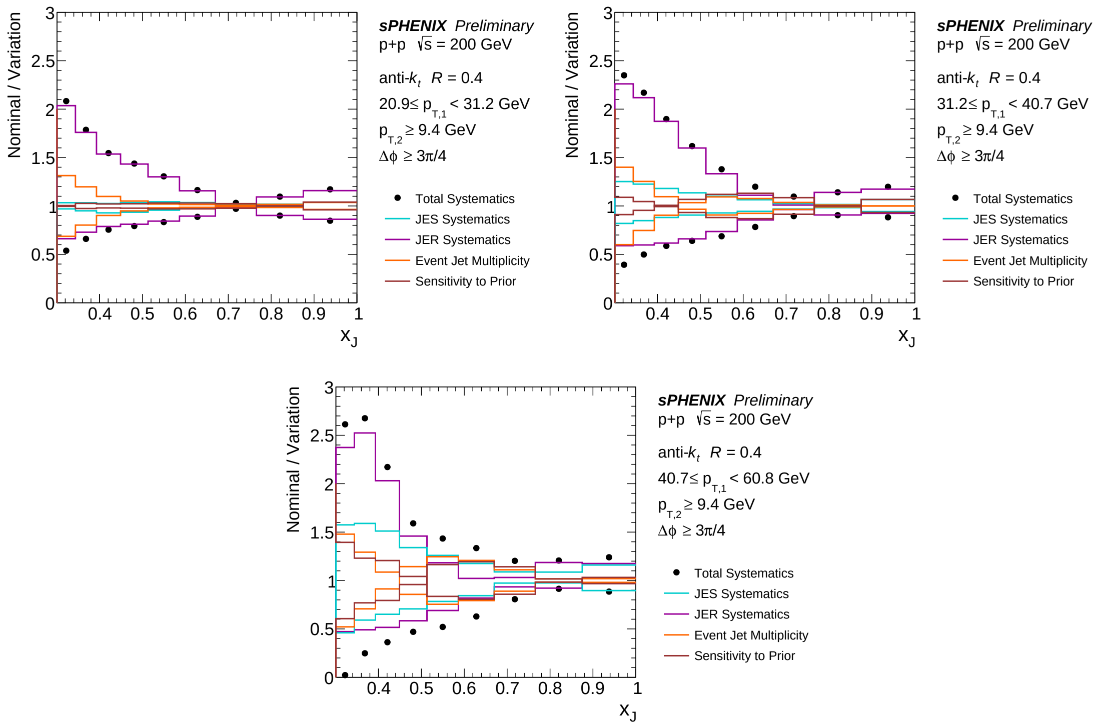

Figure 3: Total Systematic Uncertainties in x_J for three selections on $p_{T,1}$.

The systematic uncertainties included in the $\Delta\phi$ analysis are from uncertainties in (i) the JES, (ii) the JER, and (iii) the reconstruction-truth correction described in Section 3.6. The reconstruction-truth correction uncertainty includes a conservative 50% positive and negative variation on the nominal correction factor itself. Figure 4 shows all the systematic uncertainties for the $p_{T,1}$ selections added in quadrature. Figure 5 shows the same systematic uncertainties for the three $p_{T,2}$ selections.

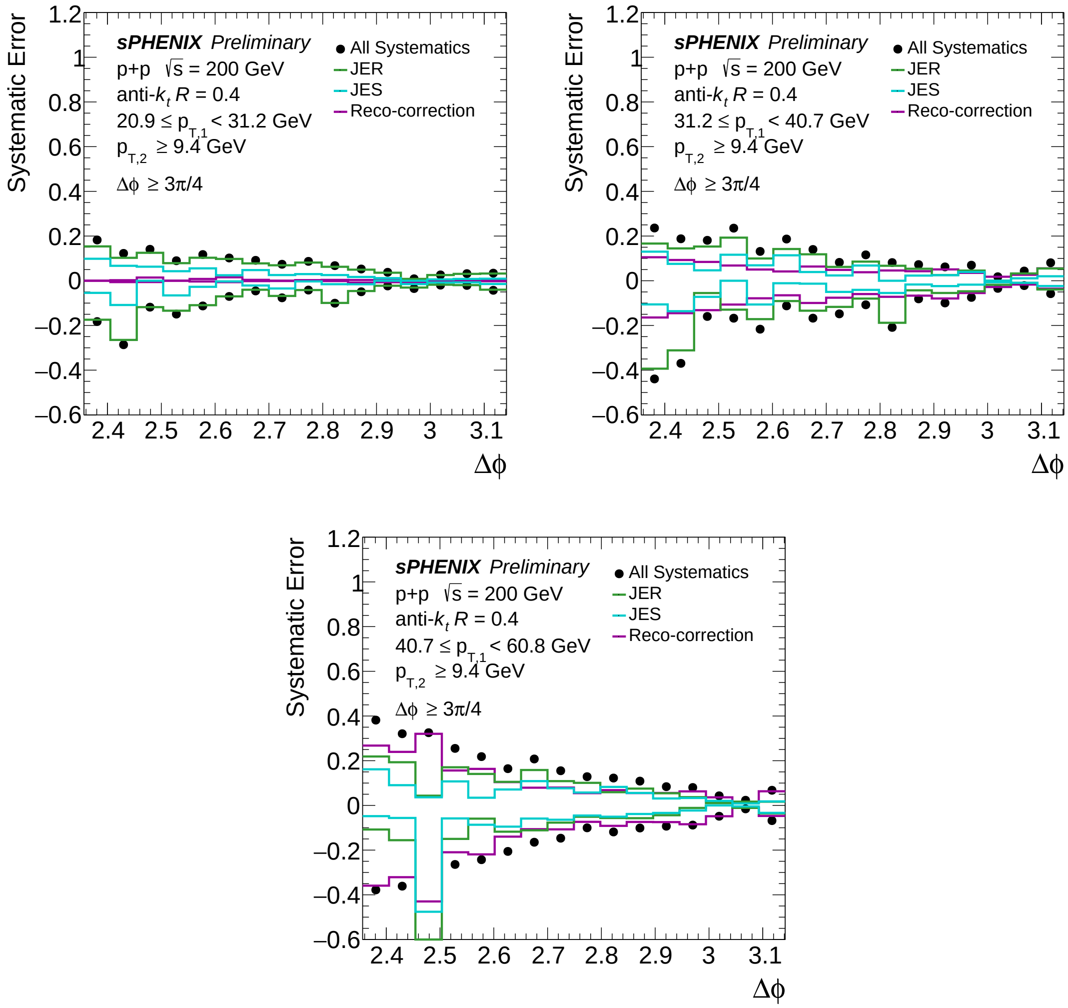

Figure 4: Total systematic uncertainties of the three $p_{T,1}$ selection in $\Delta\phi$.

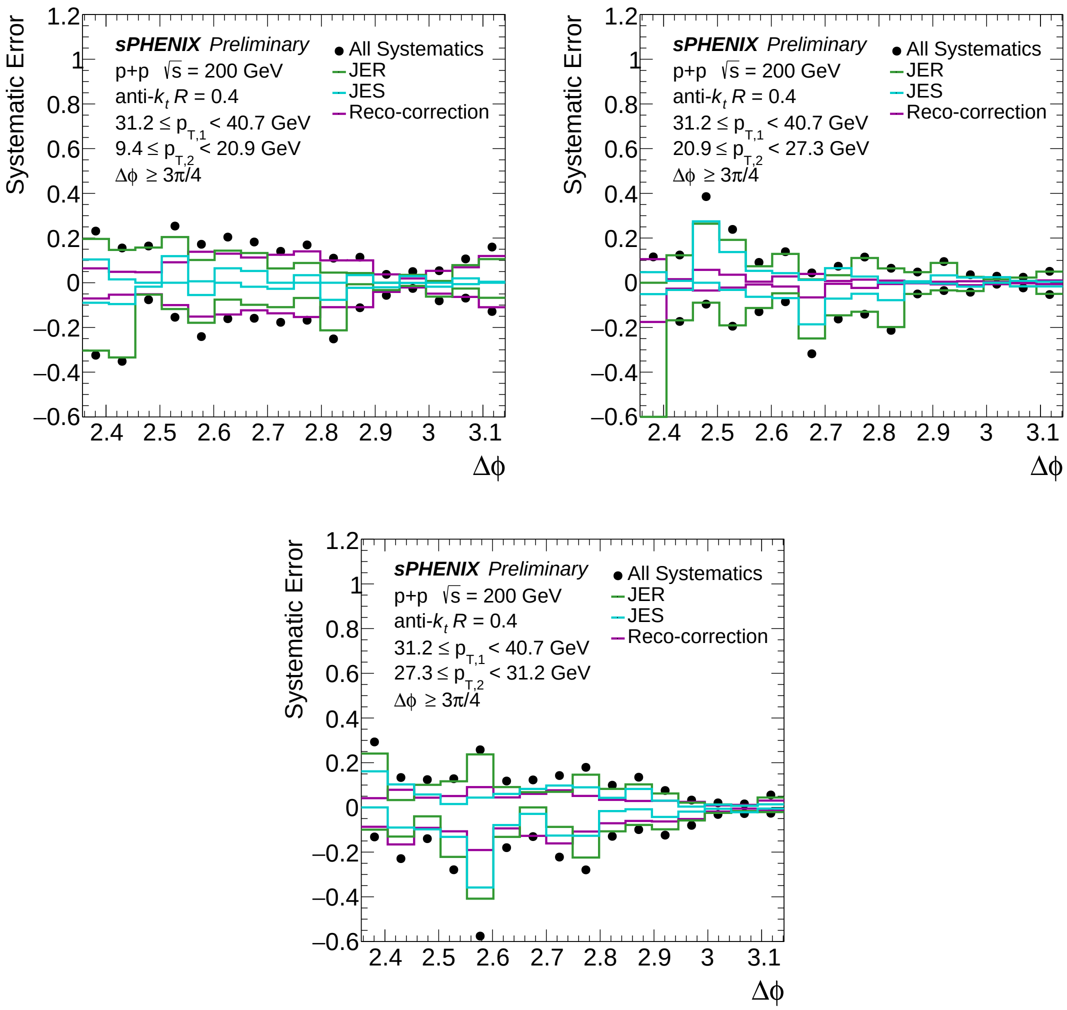

Figure 5: Total systematic uncertainties of the three $p_{T,2}$ selection in $\Delta\phi$.

5 Results

The two key observables presented here are the unfolded x_J distributions, for three selections on the leading jet p_T, and the fully corrected $\Delta\phi$ distributions in consecutive leading and subleading p_T bins.

5.1 Unfolded x_J Distributions

The reconstruction level and unfolded x_J distributions are shown in Figure 6, with three $p_{T,1}$ bins from $20.9 \leq p_{T,1} < 31.2$ GeV, $31.2 \leq p_{T,1} < 40.7$ GeV, and $40.7 \leq p_{T,1} < 60.2$ GeV with the same $p_{T,2} \geq 9.4$ GeV sub-leading cut.

Figure 7 shows the final unfolded result and comparisons with MC generators PYTHIA-8 and HERWIG-7.3. The x_J distributions are all peaked in the bin containing $x_J = 1.0$, and, at increasing $p_{T,1}$ selections, the peak becomes narrower and the distribution becomes steeper. The PYTHIA-8 predictions are in agreement with data within systematic uncertainties and follow the pattern of a more steeply peaked x_J distribution for higher p_T leading jets. The HERWIG-7.3 predictions have a less peaked x_J distribution, slightly outside the data systematic uncertainties. The dijet asymmetry in $p + p$ collisions at $\sqrt{s} = 5.02$ TeV detailed by ATLAS [9] also has a less peaked distribution from HERWIG-7.3 compared to PYTHIA-8.

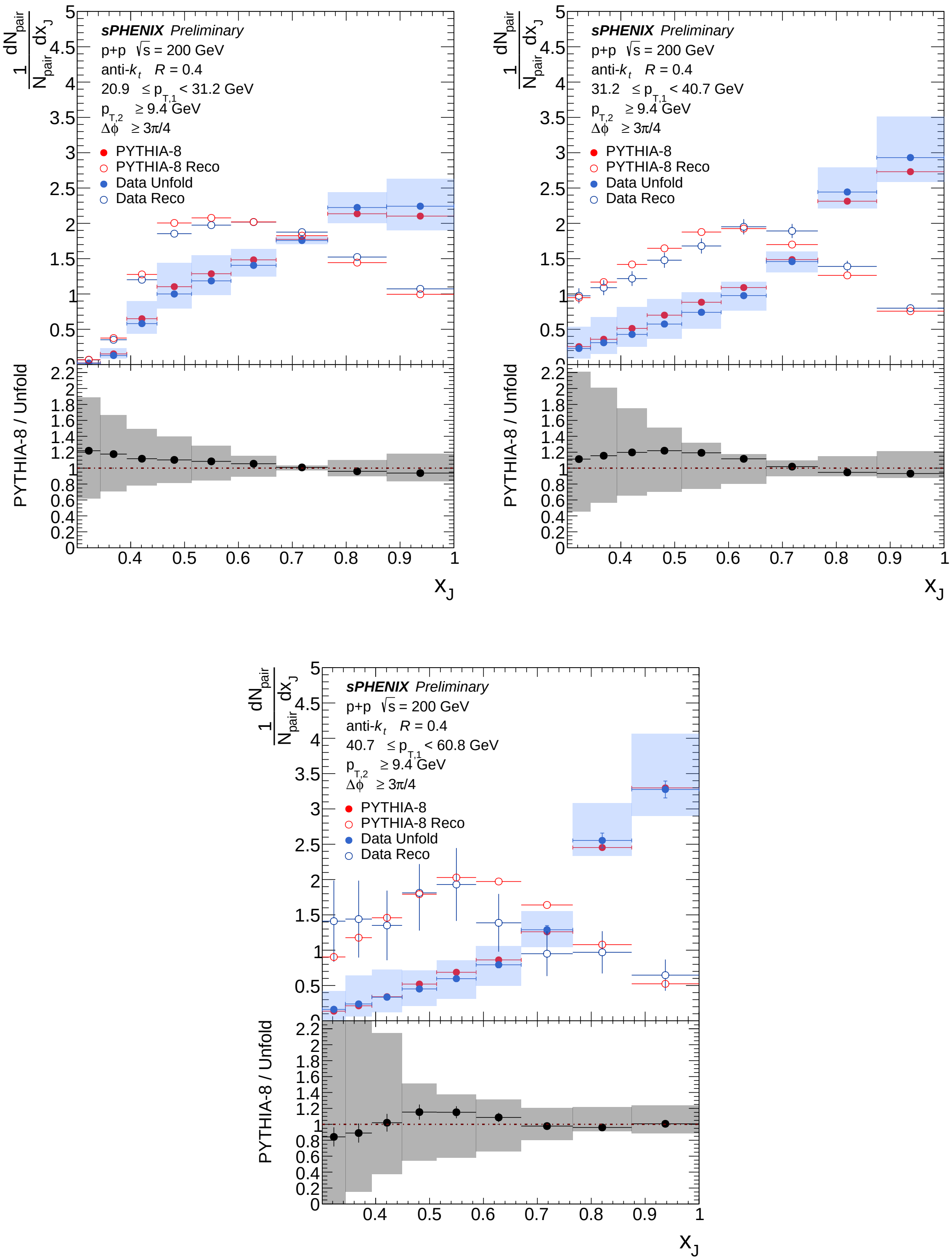

Figure 6: Reconstruction level and unfolded x_J distributions of dijet events in three leading jet $p_{T,1}$ bins. Statistical uncertainties are shown as vertical lines and systematic uncertainties as filled boxes. Also shown are results from PYTHIA-8 and the ratio of the PYTHIA-8 truth distribution to the unfolded data distribution in the lower panels.

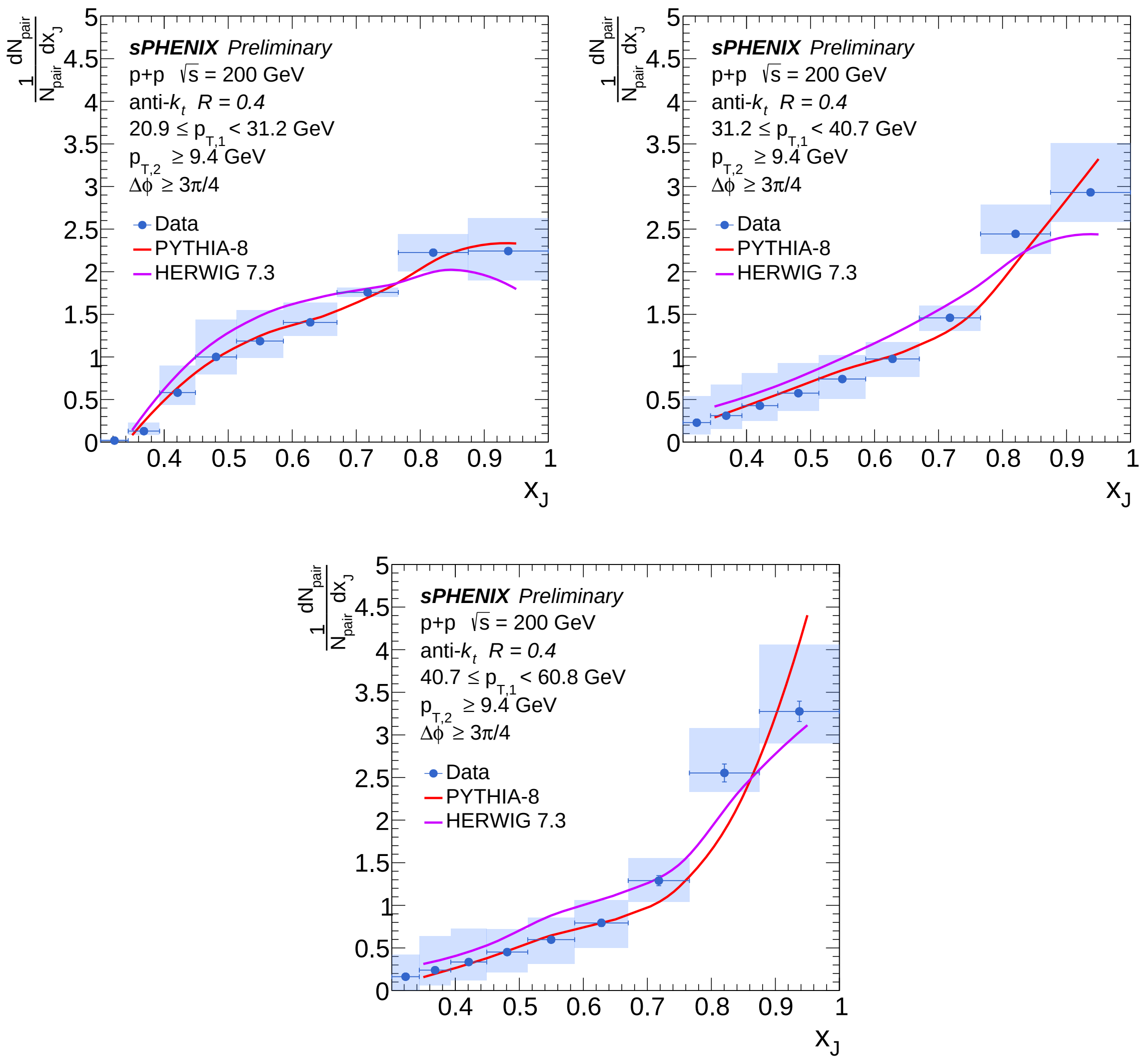

Figure 7: Fully unfolded x_J final results. Statistical uncertainties are shown as vertical lines and systematic uncertainties as filled boxes. PYTHIA-8 and HERWIG-7.3 generator results are also shown.

5.2 $\Delta\phi$ Distributions

Figure 10 shows the corrected acoplanarity in data compared with PYTHIA-8 results in leading $20.9 \leq p_{T,1} < 31.2$ GeV, $31.2 \leq p_{T,1} < 40.7$ GeV, and $40.7 \leq p_{T,1} < 60.2$ GeV. In increasing $p_{T,1}$ bins, the peak at π becomes more prominent and the distribution falls faster as x_J moves further from unity, which is expected. The data agree with the truth-level PYTHIA-8 results, which follow the same trend with increasing leading jet p_T.

Figure 11 shows the acoplanarity of dijets in data compared with the PYTHIA-8 and HERWIG-7.3 truth level dijets in subleading $p_{T,2}$ bins: $9.4 \leq p_{T,2} < 16.8$ GeV, $16.8 \leq p_{T,2} < 20.9$ GeV, $20.9 \leq p_{T,2} < 31.2$ GeV with the same leading $p_{T,1}$ bin $31.2 \leq p_{T,1} < 40.7$ GeV. The expected result is seen in both data, PYTHIA-8, and HERWIG-7.3 reconstructed dijets, where as the dijet becomes more balanced, and the acoplanarity is pushed closer to π. The angle at which each consecutive bin rises at $\Delta\phi = \pi$ in data agrees with reconstructed dijets.

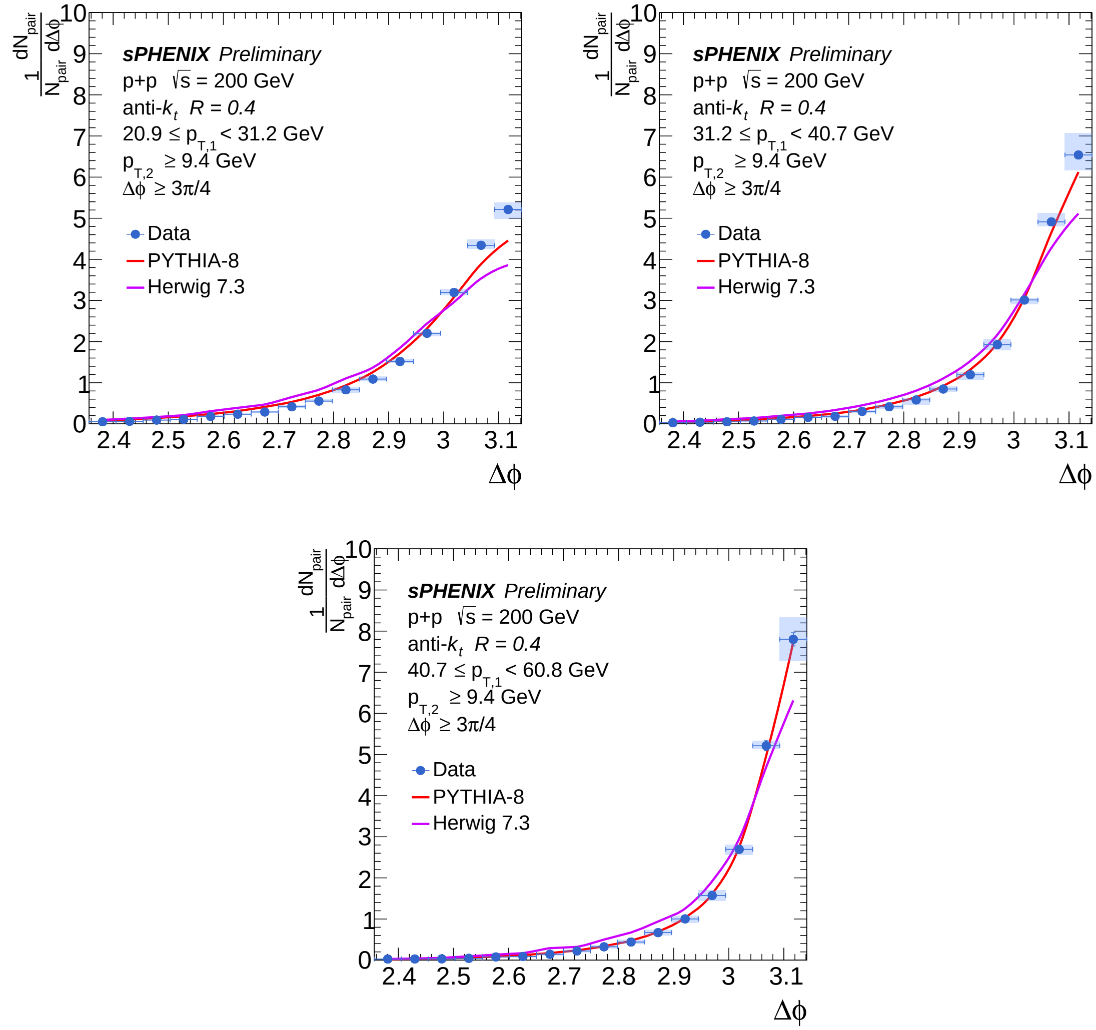

Figure 8: $\Delta\phi$ distributions for the three $p_{T,1}$ selections. Statistical uncertainties are shown as vertical lines and systematic uncertainties as filled boxes. PYTHIA-8 and HERWIG-7.3 generator results are also shown.

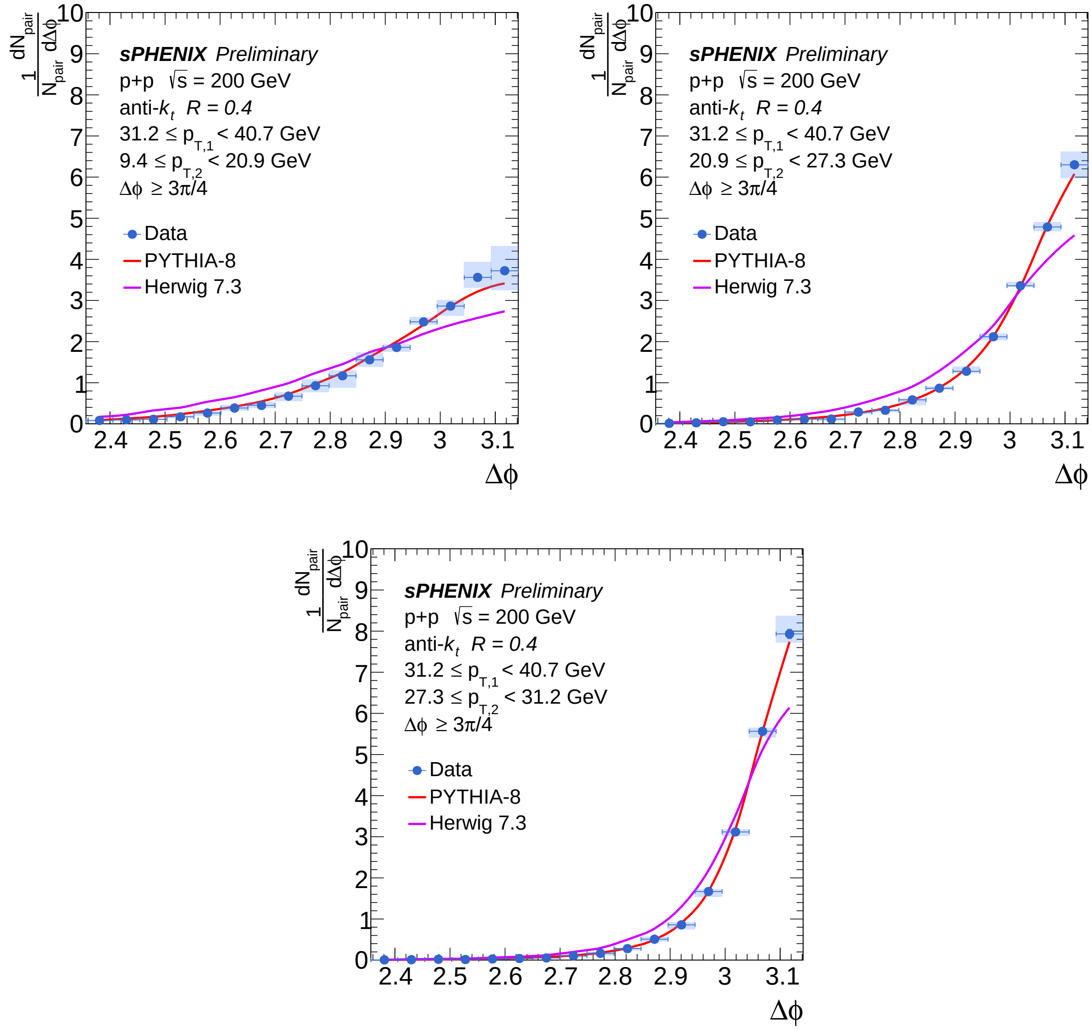

Figure 9: $\Delta\phi$ distributions for the three $p_{T,2}$ selections with the middle $p_{T,1}$ selection. Statistical uncertainties are shown as vertical lines and systematic uncertainties as filled boxes. PYTHIA-8 and HERWIG-7.3 results are also shown.

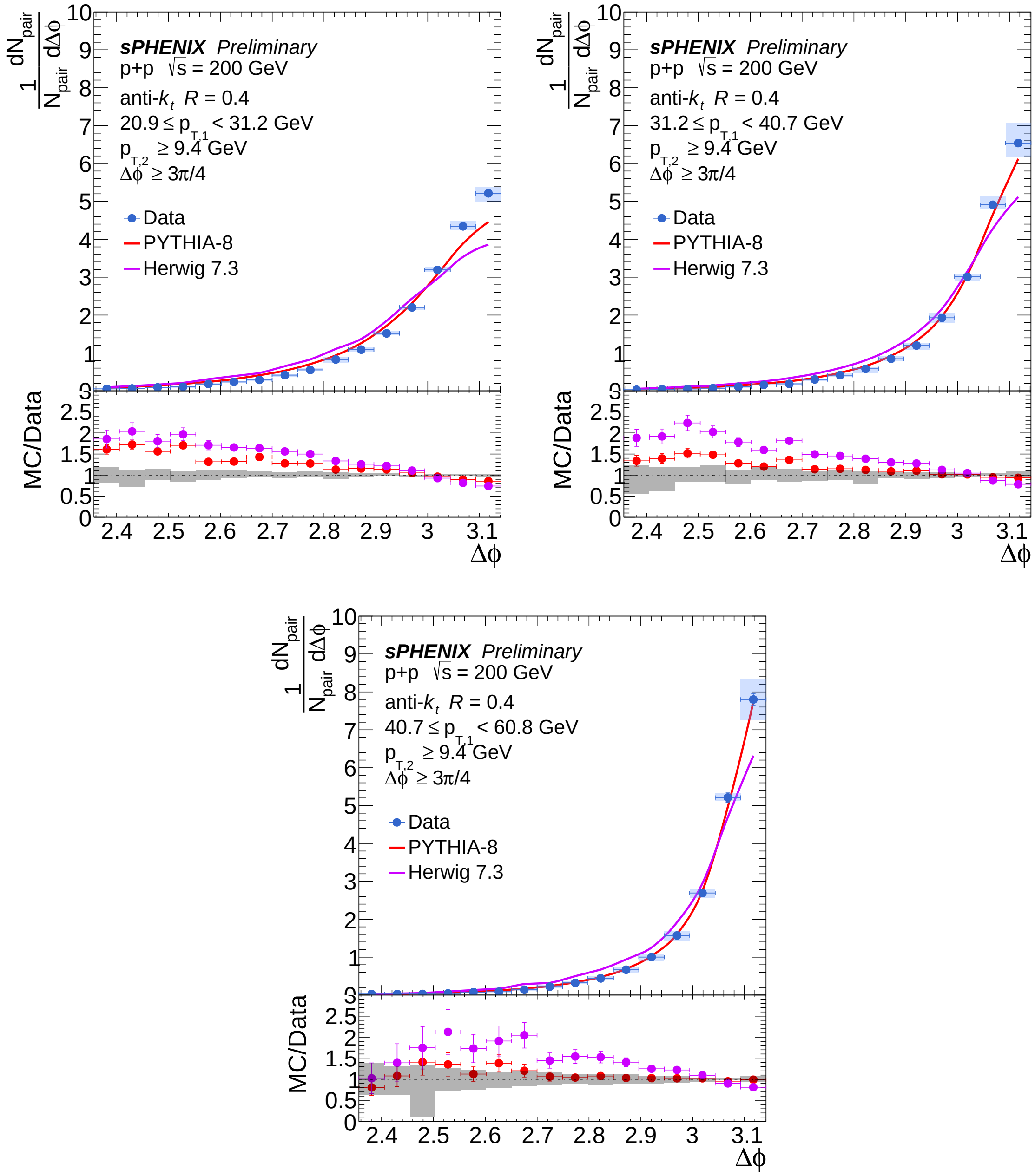

Figure 10: $\Delta\phi$ distributions for the three $p_{T,1}$ selections. Statistical uncertainties are shown as vertical lines and systematic uncertainties as filled boxes. PYTHIA-8 and HERWIG-7.3 generator results are also shown. Ratio of each generator to the data is shown on the bottom panel.

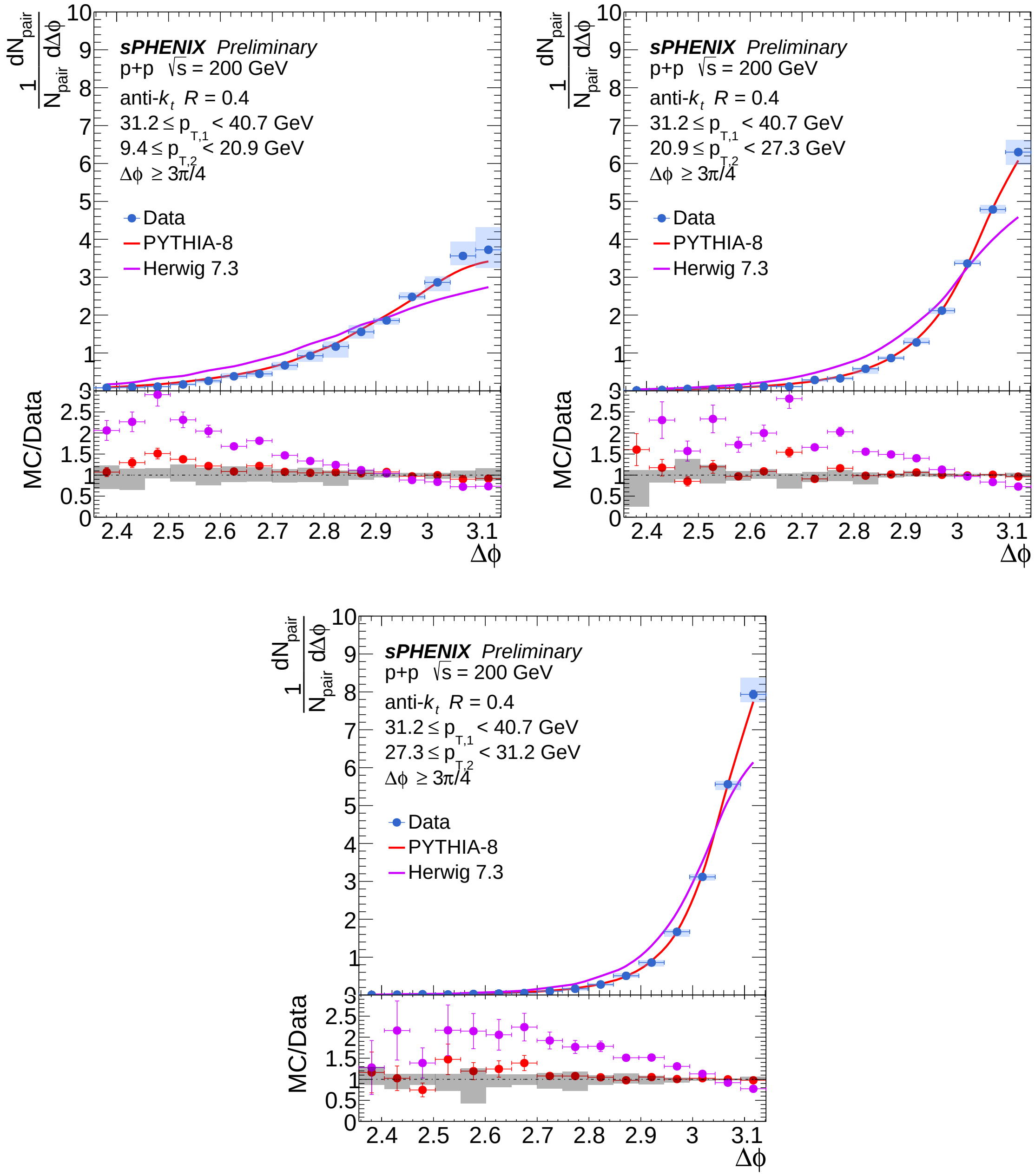

Figure 11: $\Delta\phi$ distributions for the three $p_{T,2}$ selections with the middle $p_{T,1}$ selection. Statistical uncertainties are shown as vertical lines and systematic uncertainties as filled boxes. PYTHIA-8 and HERWIG-7.3 results are also shown. Ratio of each generator to the data is shown on the bottom panel.

6 Summary

This note details the measurement of dijet imbalance (x_J) and acoplanarity ($\Delta\phi$) in $p + p$ collisions at $\sqrt{s} = 200$ GeV taken with the sPHENIX detector taken in 2024 at RHIC. Jets are reconstructed using the anti-k_t algorithm with $R = 0.4$ from calorimeter energy information. Exclusive selections are made on leading jets with $20.9 \leq p_{T,1} < 31.2$ GeV, $31.2 \leq p_{T,1} < 40.7$ GeV, and $40.7 \leq p_{T,1} < 60.2$ GeV and subleading jets with $p_{T,2} > 9.4$ GeV opposite the leading jet ($\Delta\phi > 3\pi/4$). The distribution of $x_J = p_{T,2}/p_{T,1}$ is calculated and unfolded for detector effects back to the truth-particle level distribution. These unfolded results are compared with the MC calculations PYTHIA-8 and HERWIG-7.3. There is good agreement within uncertainties between the MC and experimental data. The x_J and $\Delta\phi$ distributions peak more sharply at unity and π, respectively, as the leading jet $p_{T,1}$ increases.

A Jet Energy Resolution

The jet energy resolution (JER) is determined via a data-driven dijet bisector method [29]. First, events are selected that have only a leading and sub-leading jet, i.e., no additional jets with $p_T > 3$ GeV, that are within the acceptance of the sPHENIX detector. The two jets' $\vec{p_T}$ are added only considering their p_T and ϕ kinematics. Figure 12 (reproduced from Ref. [29]) shows this process.

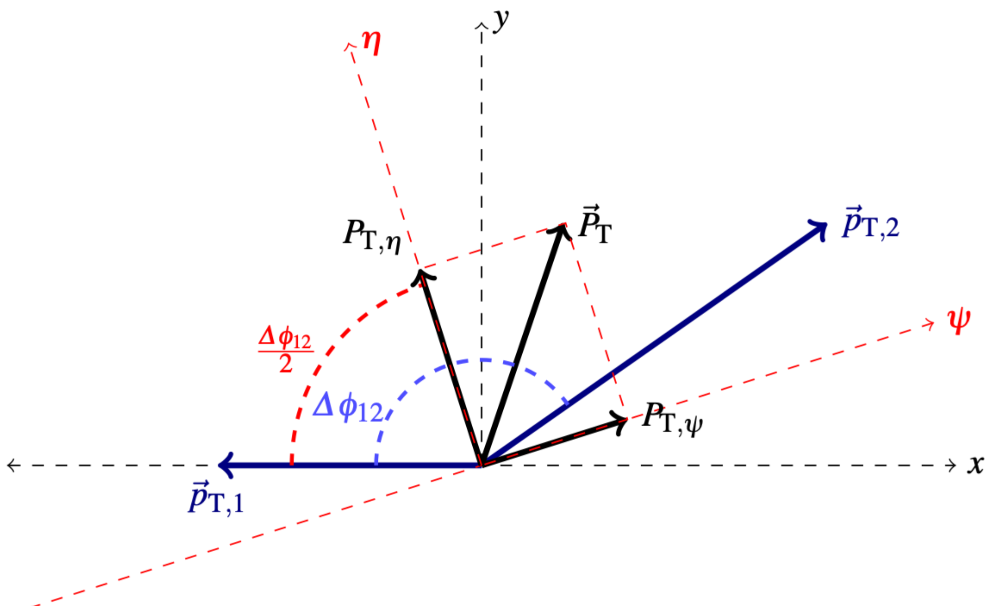

Figure 12: Diagram of leading $\vec{p_{T,1}}$ and subleading $\vec{p_{T,2}}$ jets in the coordinate system used for the bisector method (reproduced from Ref. [29]).

The vector sum $\vec{p_T}^{dijet}$ is broken down into two components: $p_{T\eta}$, that is parallel to the bisector of the dijet ($\frac{\Delta\phi_{12}}{2}$ away from the leading and subleading jet), and $p_{T\psi}$, that is orthogonal. For each bin in average p_T, the distributions of the $p_{T\eta}$ and $p_{T\psi}$ are fitted with a Gaussian function to extract their widths $\sigma(p_{T\eta})$ and $\sigma(p_{T\psi})$. The orientation of the two jets is randomized to symmetrize the distributions. Figure 13 shows the widths $\sigma(p_{T\eta})$ and $\sigma(p_{T\psi})$ as a function of $\langle p_T \rangle$ in PYTHIA-8 dijets, as well as in reconstructed PYTHIA-8 dijets and in data. Both the $p_{T\eta}$ and $p_{T\psi}$ components are sensitive to initial-state radiation, which is isotropic. This is shown in the similarity of $\sigma(p_{T\eta})$ and $\sigma(p_{T\psi})$ in truth level PYTHIA-8, where there is only a 1 GeV difference between the two components' widths. The $\sigma(p_{T\psi})$ component is always wider due to the dijet $\Delta\phi$ selection, such that the hard radiation escaping the jet cone, contributing to larger dijet imbalance, will widen the more transverse component ψ. This is also seen in the PYTHIA-8 distribution. However, the effects of the resolution are larger in the $p_{T\psi}$ component of $\vec{p_T}^{dijet}$. This can be seen in Figure 13 as $\sigma(p_{T\psi})$ in the reconstructed PYTHIA-8 dijets increases to $7-8$ GeV from the truth level PYTHIA-8 dijets, while $\sigma(p_{T\eta})$ remains unchanged. Also, from the larger width $\sigma(p_{T\psi})$ in data, the resolution in data must be underestimated by what is represented in our reconstruction.

Using these values, the jet energy resolution can be determined as a function of $\langle p_T \rangle$ using Equation 1 for data and reconstructed PYTHIA-8 jets separately.

$$\frac{\sigma(p_T)}{p_T} = \frac{\sigma(p_{T,\psi}) \ominus \sigma(p_{T,\eta})}{\sqrt{2} < p_T > \sqrt{< |\cos\Delta\phi| >}} \tag{1}$$

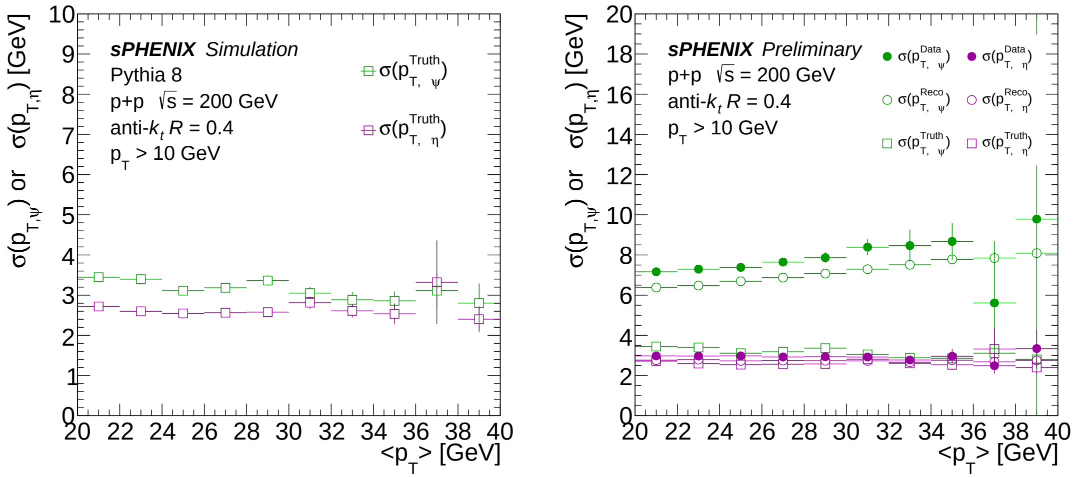

Figure 13: (Left) PYTHIA-8 truth dijet $\sigma(p_{T\psi})$ and $\sigma(p_{T\eta})$ as a function of $\langle p_T \rangle$ and (right) includes $\sigma(p_{T\psi})$ and $\sigma(p_{T\eta})$ in reconstructed PYTHIA-8 jets and data.

The limitation of this method is that there are final-state radiation effects that contribute additional and unequal contribution to the $p_{T\psi}$ width. Monte Carlo studies with PYTHIA-8 were performed to study these limitations. Figure 14 shows the result of this analysis. The resulting JER is approximately 10% larger than the one derived purely from the simulation. The fit follows Equation 2.

$$\frac{\sigma(p_T)}{p_T} = C \oplus \frac{S}{\sqrt{p_T}} \oplus \frac{N}{p_T} \tag{2}$$

In this equation, C is the constant term, S is the stochastic term, and N is the noise term. Thus, for the default response matrix, the jet energies at the reconstruction level are smeared with an additional 10% to best match the real detector performance.

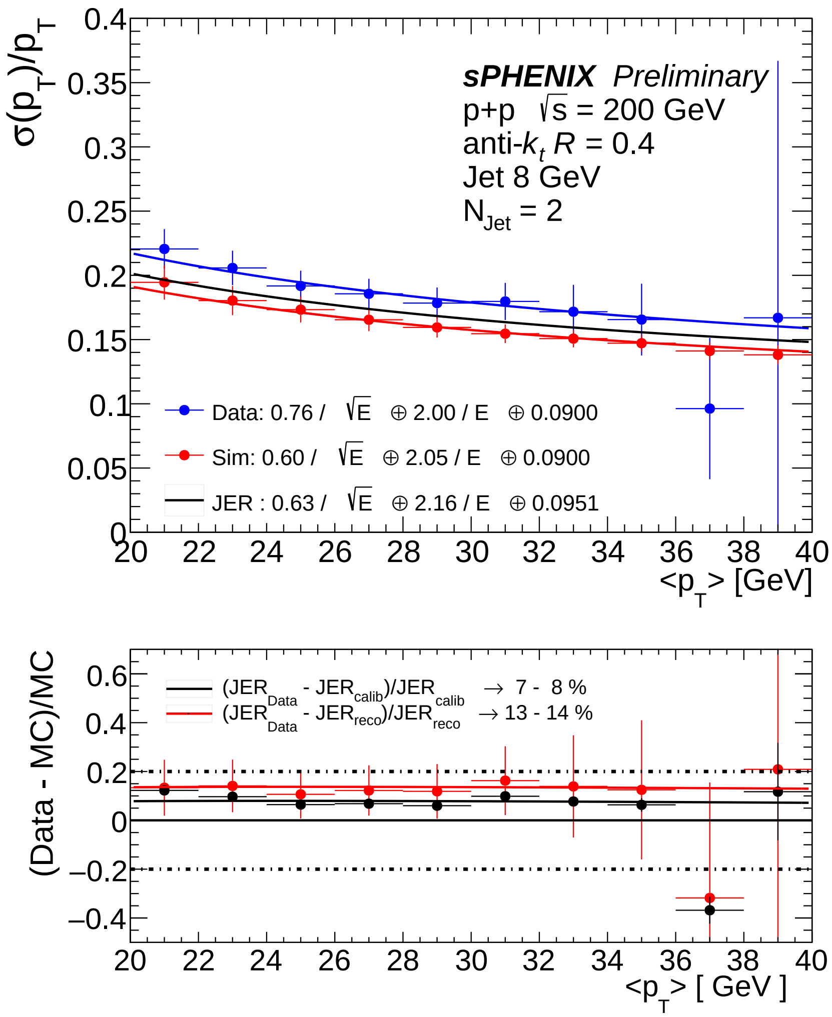

Figure 14: (top) Jet energy resolution in data and simulation derived form the bisector method as a function of average p_T with fits and the JER function retrieved from simulation based calibration. (Bottom) The ratio of each average p_T bin in Data and MC as well as the ratio of the fit to the data to the calibration result of the JER function.

References

[1] Leticia Cunqueiro and Anne M. Sickles. Studying the QGP with Jets at the LHC and RHIC. *Prog. Part. Nucl. Phys.*, 124:103940, 2022. arXiv:2110.14490, doi:10.1016/j.ppnp.2022.103940. 1

[2] G. Aad et al (ATLAS Collaboration). Observation of a Centrality-Dependent Dijet Asymmetry in Lead-Lead Collisions at $\sqrt{s_{NN}} = 2.77$ TeV with the ATLAS Detector at the LHC. *Phys. Rev. Lett.*, 105:252303, 2010. arXiv:1011.6182, doi:10.1103/PhysRevLett.105.252303. 1

[3] Guang-You Qin and Berndt Muller. Explanation of Di-jet asymmetry in Pb+Pb collisions at the Large Hadron Collider. *Phys. Rev. Lett.*, 106:162302, 2011. [Erratum: Phys.Rev.Lett. 108, 189904 (2012)]. arXiv:1012.5280, doi:10.1103/PhysRevLett.106.162302. 1

[4] José Guilherme Milhano and Korinna Christine Zapp. Origins of the di-jet asymmetry in heavy ion collisions. *Eur. Phys. J. C*, 76(5):288, 2016. arXiv:1512.08107, doi:10.1140/epjc/s10052-016-4130-9. 1

[5] S. Chatrchyan et al (CMS Collaboration). Observation and studies of jet quenching in PbPb collisions at nucleon-nucleon center-of-mass energy = 2.76 TeV. *Phys. Rev. C*, 84:024906, 2011. arXiv:1102.1957, doi:10.1103/PhysRevC.84.024906. 1

[6] S. Chatrchyan et al (CMS Collaboration). Jet Momentum Dependence of Jet Quenching in PbPb Collisions at $\sqrt{s_{NN}} = 2.76$ TeV. *Phys. Lett. B*, 712:176–197, 2012. arXiv:1202.5022, doi:10.1016/j.physletb.2012.04.058. 1

[7] M. Aaboud et al (ATLAS Collaboration). Measurement of jet p_{T} correlations in Pb+Pb and pp collisions at $\sqrt{s_{\mathrm{NN}}} = 2.76$ TeV with the ATLAS detector. *Phys. Lett. B*, 774:379–402, 2017. arXiv:1706.09363, doi:10.1016/j.physletb.2017.09.078. 1

[8] G. Aad et al (ATLAS Collaboration). Measurements of the suppression and correlations of dijets in Pb+Pb collisions at sNN=5.02 TeV. *Phys. Rev. C*, 107(5):054908, 2023. [Erratum: Phys.Rev.C 109, 029901 (2024)]. arXiv:2205.00682, doi:10.1103/PhysRevC.107.054908. 1, 3.4

[9] G. Aad et al (ATLAS Collaboration). Jet radius dependence of dijet momentum balance and suppression in Pb+Pb collisions at 5.02 TeV with the ATLAS detector. *Phys. Rev. C*, 110(5):054912, 2024. arXiv:2407.18796, doi:10.1103/PhysRevC.110.054912. 1, 5.1

[10] Francesco D'Eramo, Krishna Rajagopal, and Yi Yin. Molière scattering in quark-gluon plasma: finding point-like scatterers in a liquid. *JHEP*, 01:172, 2019. arXiv:1808.03250, doi:10.1007/JHEP01(2019)172. 1

[11] A. Adare et al. An Upgrade Proposal from the PHENIX Collaboration. 1 2015. arXiv:1501.06197. 1, 2

[12] Ron Belmont et al. Predictions for the sPHENIX physics program. *Nucl. Phys. A*, 1043:122821, 2024. arXiv:2305.15491, doi:10.1016/j.nuclphysa.2024.122821. 1, 2

[13] L. Adamczyk et al (STAR Collaboration). Dijet imbalance measurements in $Au + Au$ and pp collisions at $\sqrt{s_{NN}} = 200$ GeV at STAR. *Phys. Rev. Lett.*, 119(6):062301, 2017. arXiv:1609.03878, doi:10.1103/PhysRevLett.119.062301. 1

[14] M. Harrison, T. Ludlam, and S. Ozaki. RHIC project overview. *Nucl. Instrum. Meth. A*, 499(2):235–244, 2003. doi:10.1016/S0168-9002(02)01937-X. 2

[15] The sPHENIX Collaboration. sPHENIX Technical Design Report, PD-2/3 Release, 2019. URL: https://indico.bnl.gov/event/7081/attachments/25527/38284/sphenixtdr20190513.pdf. 2

[16] Henry Klest. Overview and design of the sPHENIX TPC. *J. Phys. Conf. Ser.*, 1498:012025, 2020. arXiv:2110.02082, doi:10.1088/1742-6596/1498/1/012025. 2

[17] S. Aune et al. The sPHENIX Micromegas Outer Tracker. *Nucl. Instrum. Meth. A*, 1066:169615, 2024. doi:10.1016/j.nima.2024.169615. 2

[18] C. A. Aidala et al. Design and Beam Test Results for the 2-D Projective sPHENIX Electromagnetic Calorimeter Prototype. *IEEE Trans. Nucl. Sci.*, 68(2):173–181, 2021. doi:10.1109/TNS.2020.3034643. 2

[19] C. A. Aidala et al. Design and Beam Test Results for the sPHENIX Electromagnetic and Hadronic Calorimeter Prototypes. *IEEE Trans. Nucl. Sci.*, 65(12):2901–2919, 2018. doi:10.1109/TNS.2018.2879047. 2

[20] T. G. O'Connor et al. Design and testing of the 1.5 T superconducting solenoid for the BaBar detector at PEP-II in SLAC. *IEEE Trans. Appl. Supercond.*, 9:847–851, 1999. doi:10.1109/77.783429. 2

[21] Torbjörn Sjöstrand et al. An introduction to PYTHIA 8.2. *Comput. Phys. Commun.*, 191:159–177, 2015. arXiv:1410.3012, doi:10.1016/j.cpc.2015.01.024. 3.2

[22] Manny Rosales Aguilar et al. PYTHIA 8 underlying event tune for RHIC energies. *Phys. Rev. D*, 105(1):016011, 2022. arXiv:2110.09447, doi:10.1103/PhysRevD.105.016011. 3.2

[23] S. Agostinelli et al. Geant4—a simulation toolkit. *Nuclear Instruments and Methods in Physics Research Section A: Accelerators, Spectrometers, Detectors and Associated Equipment*, 506(3):250–303, 2003. doi:10.1016/S0168-9002(03)01368-8. 3.2, 3.5

[24] Gavin Bewick et al. Herwig 7.3 release note. *Eur. Phys. J. C*, 84(10):1053, 2024. arXiv:2312.05175, doi:10.1140/epjc/s10052-024-13211-9. 3.2

[25] Umar Sohail Qureshi, Raghav Kunnawalkam Elayavalli, Luke Mozarsky, Helen Caines, and Isaac Mooney. A New Herwig7 Underlying Event Tune: from RHIC to LHC Energies. 11 2024. arXiv:2411.16897. 3.2

[26] Matteo Cacciari, Gavin P. Salam, and Gregory Soyez. FastJet User Manual. *Eur. Phys. J. C*, 72:1896, 2012. arXiv:1111.6097, doi:10.1140/epjc/s10052-012-1896-2. 3.3

[27] G. D'Agostini. Improved iterative bayesian unfolding, 2010. URL: https://arxiv.org/abs/1010.0632, arXiv:1010.0632. 3.5

[28] Tim Adye. Unfolding algorithms and tests using RooUnfold. In *PHYSTAT 2011*, pages 313–318, Geneva, 2011. CERN. arXiv:1105.1160, doi:10.5170/CERN-2011-006.313. 3.5

[29] G. Aad et al (ATLAS Collaboration). Jet energy resolution in proton-proton collisions at $\sqrt{s} = 7$ TeV recorded in 2010 with the atlas detector. *The European Physical Journal C*, 73(3), March 2013. URL: http://dx.doi.org/10.1140/epjc/s10052-013-2306-0, doi:10.1140/epjc/s10052-013-2306-0. A, 12